Study on valley polarization and quantum properties of two-dimensional $Pt_4Hg_2Cl_3X_3$ (X = F, Br)

Yuxian Yang(杨宇贤)[1,3,†], Yu Ding(丁宇)[2,†], Jinniu Tao(陶金牛)[1], Hua Che(车华)[1], Fawei Wang(王发威)[1], and Changwen Zhang(张昌文)[3,‡]

[1] *Aviation Maintenance NCO Academy, Air Force Engineering University, Xinyang* 464000, *China*
[2] *School of Physics, Shandong University, Jinan* 250100, *China*
[3] *School of Physics and Technology, University of Jinan, Jinan* 250022, *China*

(Received 6 October 2025; revised manuscript received 23 November 2025; accepted manuscript online 15 December 2025)

The quantum anomalous valley Hall effect (QAVHE) represents an important research direction in topological electronics. In this work, based on first-principles calculations combined with a tight-binding (TB) model, we predict that the two-dimensional (2D) ferromagnetic material $Pt_4Hg_2Cl_3X_3$ (X = F, Br) can realize the QAVHE. The system exhibits a Curie temperature of 219 K, and its magnetic easy axis can be tuned from the in-plane to the out-of-plane direction under biaxial strain, leading to a remarkable change in valley polarization and enabling effective control of the valley degree of freedom. A strain-driven topological phase transition from a trivial to a nontrivial state is revealed, resulting in the coexistence of the anomalous valley Hall effect (AVHE) and the quantum anomalous Hall effect (QAHE), characterized by a Chern number ($C = 1$) and chiral spin–valley–locked states. The coexistence of robust valley polarization and a high Curie temperature makes this system an ideal platform for realizing dissipationless electronic transport and topological quantum computation, offering valuable prospects for the development of valleytronics, spintronics, and topological quantum materials.

Keywords: valley polarization, topological phase transition, quantum anomalous valley Hall effect, first-principles calculations

PACS: 71.15.Mb, 73.43.–f, 73.63.–b

DOI: 10.1088/1674-1056/ae2c6a **CSTR:** 32038.14.CPB.ae2c6a

1. Introduction

With the rapid progress in the study of two-dimensional (2D) materials, both the types and quantities of 2D valley systems have significantly increased,[1–4] and substantial advances have been achieved in understanding their fundamental properties and manipulating their quantum characteristics. In particular, 2D hexagonal lattices, such as transition-metal dichalcogenides (TMDs), have been regarded as promising candidates for controlling charge, spin, and valley degrees of freedom.[5–11] In these materials, the breaking of spatial inversion symmetry allows the exploration of valley-contrasting phenomena, such as the valley Hall effect (VHE) and valley-controllable optical selection rules.[12,13] In recent years, progress in valleytronics has emphasized the generation of valley polarization by breaking time-reversal symmetry, thereby lifting the degeneracy of the K and K' valleys.[14] Several approaches have been proposed, including optical pumping,[15–17] magnetic doping,[18–20] magnetic proximity effects,[21–23] applying external magnetic fields,[24–27] as well as edges,[28] defects,[29] and intervalley scattering.[30,31] Building on these efforts, Hu *et al.* introduced the concept of the quantum anomalous valley Hall effect,[32,33] in which valley polarization coexists with the quantum anomalous Hall effect (QAHE). Compared with the anomalous valley Hall effect (AVHE), the QAVHE is characterized by a nonzero Chern number ($C = 1$) and chiral spin–valley locking, endowing it with intrinsic importance and practical relevance. Since then, several 2D systems have been theoretically predicted to possess QAVHE properties, including $FeCl_2$,[34] VSi_2N_4,[35] VSi_2P_4,[36,37] FeClF,[38] and MBr_2 (M = Ru, Os).[39,40] Nevertheless, the number of available valley materials that simultaneously combine valley physics with topological physics remains very limited. Most of the studies to date are still restricted to monolayer transition-metal binary compounds with 2H phases or VA_2Z_4-type (A = Si, Ge; Z = N, P) structures, such as VSi_2N_4 and VSi_2P_4. Furthermore, although progress has been made in both AVHE and QAHE, valley polarization in intrinsically ferromagnetic (FM) 2D materials is usually weak, rendering them vulnerable to thermal fluctuations at room temperature and thus limiting their practical applications. Therefore, it is crucial to identify systems that can simultaneously realize out-of-plane magnetic anisotropy, stable valley polarization, and high Curie temperatures.

Jacutingaite (Pt_2HgSe_3), a layered platinum-group min-

†These authors contributed equally to this work.
‡Corresponding author. E-mail: ss_zhangchw@ujn.edu.cn

© 2026 Chinese Physical Society and IOP Publishing Ltd. All rights, including for text and data mining, AI training, and similar technologies, are reserved.

CPB Online In-Press

eral discovered in Brazil by Cabral *et al.*,[41–43] crystallizes in space group $P3m1$ (No. 164) with a triangular primitive cell composed of 12 atoms. Its atomic configuration forms a sandwich-like structure in which a Pt layer is embedded between two Hg/Se layers. Interestingly, the Hg atoms at the top and bottom layers form a distorted honeycomb lattice, leading to two Dirac bands whose Dirac points lie exactly at the Fermi level, resembling the band structure of graphene. When spin–orbit coupling (SOC) is included, a band gap of 0.15 eV opens at the K point, thereby enabling the realization of the quantum spin Hall effect in this material. Shortly thereafter, scanning tunneling microscopy (STM) measurements confirmed the existence of the gap and the hallmark edge states.[43] Consequently, 2D jacutingaite was identified as a Kane–Mele quantum spin Hall insulator.[44] Compared with graphene, it exhibits significantly stronger SOC and a larger band gap. Theoretical studies further confirmed that monolayer Pt_2HgSe_3 is a dynamically stable topological insulator with a band gap of about 0.5 eV.[44] This material has already been successfully synthesized and demonstrates broad application potential in nanoelectronics and spintronics. Inspired by these findings, we propose a novel 2D structure, $Pt_4Hg_2Cl_3X_3$ (X = F, Br), and systematically investigate its structural stability, magnetic properties, electronic band structure, and topological features. First-principles calculations reveal that monolayer $Pt_4Hg_2Cl_3X_3$ (X = F, Br) exhibits intrinsic ferromagnetism, with a magnetic moment of 6 μ_B per unit cell. When the magnetic easy axis is oriented out of the plane, pronounced differences in the valley polarization values emerge, thereby enhancing the tunability of the valley degrees of freedom. Moreover, the calculated edge-state density maps, Berry curvature, and anomalous Hall conductivity confirm that monolayer $Pt_4Hg_2Cl_3X_3$ (X = F, Br) supports the QAVHE, highlighting its promise for nondissipative valleytronic devices. Although the easy axis is initially in-plane, strain engineering can induce a transition of the magnetic anisotropy from in-plane to out-of-plane, leading to significant energy splitting at the K/K' valleys and the emergence of valley polarization. This enhanced controllability of the valley degrees of freedom further stabilizes the QAVHE, as corroborated by the computed edge states, Berry curvature, and anomalous Hall conductivity. Taken together, these results establish monolayer $Pt_4Hg_2Cl_3X_3$ (X = F, Br) as one of the most promising next-generation valleytronic and topological materials for realizing dissipationless electronic devices.

2. Computational details

First-principles calculations were carried out using the Vienna *ab initio* simulation package (VASP),[45–47] which is based on density functional theory (DFT).[48] The exchange–correlation interactions between electrons were treated within the generalized gradient approximation (GGA) in the Perdew–Burke–Ernzerhof (PBE) scheme.[49] The plane-wave cutoff energy was set to 520 eV, and the Brillouin zone was sampled with a $13 \times 13 \times 1$ Monkhorst–Pack k-mesh. Structural relaxations were performed until the residual forces on each atom were less than 0.01 eV/Å and the total energy convergence criterion was set to 10^{-8} eV. To eliminate spurious interactions between periodic images, a vacuum spacing of 20 Å was introduced along the z direction. The phonon dispersion spectra were calculated using the supercell approach implemented in the PHONOPY code. For the Pt-d electrons, the on-site Coulomb interaction was considered by employing the DFT+U method with an effective U value of 3 eV.[50] Furthermore, the Berry curvature was obtained by constructing maximally localized Wannier functions (MLWFs)[51] with the aid of the WANNIER90 package, and the edge-state spectra were investigated using the iterative Green's function method. Based on the tight-binding Hamiltonian constructed from the MLWFs, the Chern number was further evaluated. Furthermore, the edge-state spectra were investigated using the iterative Green's function approach.[51,52]

3. Results and discussion

We first investigated the geometric structure and stability of the pristine monolayer $Pt_4Hg_2Cl_3X_3$ (X = F, Br). The optimized 2D $Pt_4Hg_2Cl_3X_3$ possesses a centrosymmetric hexagonal lattice belonging to the space group $P3m1$. The top and side views of the structure are presented in Figs. 1(a) and 1(b). The fully relaxed lattice constants are 7.33 Å and 7.72 Å, respectively. Each unit cell contains four Pt atoms, which can be classified into two categories according to their local environment. One type of Pt atom is coordinated with nonmetal atoms (Cl and X), whereas the other type resides at the center of a planar quadrilateral formed by Cl and X atoms and bonds with Hg atoms. To further analyze the bonding characteristics, we calculated the electron localization function (ELF). As shown in Fig. S1 of the supporting information, the electron localization is mainly distributed around Cl and X atoms, confirming that $Pt_4Hg_2Cl_3X_3$ is essentially an ionic-type compound. In addition, the phonon dispersion spectrum was computed to evaluate the dynamical stability of the structure. As illustrated in Fig. 1(c), no imaginary frequencies are observed throughout the Brillouin zone, indicating that the system is dynamically stable.

Furthermore, we calculated the cohesive energy of the structure, which is defined as the energy required to decompose the condensed system into isolated free atoms. The cohesive energy is one of the most important physical parameters for quantifying the stability of a material. The cohesive energy per atom can be expressed as[53]

$$\Delta E_{\mathrm{coh}} = E_{\mathrm{Pt}} + E_{\mathrm{Hg}} + E_{\mathrm{Cl}} + E_X - E_{\mathrm{Pt_4Hg_2Cl_3X_3}}, \quad (1)$$

CPB Online In Press

where E_{Pt}, E_{Hg}, E_{Cl}, and E_X correspond to the energies of Pt, Hg, Cl, and F/Br atoms, respectively, and $E_{\mathrm{Pt_4Hg_2Cl_3}X_3}$ is the energy of a single-cell $\mathrm{Pt_4Hg_2Cl_3}X_3$. The calculated cohesive energies for F and Br are 2.03 eV and 3.17 eV, respectively. These relatively high cohesive energies indicate strong bonding interactions within the lattice, confirming not only the structural stability but also the experimental feasibility of synthesizing $\mathrm{Pt_4Hg_2Cl_3}X_3$. To gain deeper insights into the physical mechanism of the quantum anomalous Hall (QAH) effect induced by halogen functionalization, we constructed a tight-binding (TB) model to qualitatively describe the SOC-driven bandgap opening and its evolution.[54–57] Unlike conventional studies, our model introduces a magnetization term into a four-band Hamiltonian defined on a hexagonal lattice, owing to the intrinsic ferromagnetism of halogen-functionalized jacutingaite. The Hamiltonian with intrinsic SOC can be expressed as

$$\begin{aligned} H = {} & \varepsilon_0 + \sum_{i,j\alpha} (tC^{+}_{i\alpha}C_{j\alpha} + \mathrm{h.c.}) \\ & + \mathrm{i}\lambda \sum_{i,j} C^{+}_{i} \boldsymbol{S} \cdot \left(\frac{\boldsymbol{d}_{jk}}{|\boldsymbol{d}_{jk}|} \times \frac{\boldsymbol{d}_{ki}}{|\boldsymbol{d}_{ki}|} \right) C_j \\ & + M \sum_{i,\alpha,\beta} C^{+}_{i\alpha} S^{z}_{\alpha\beta} C_{i\beta}, \end{aligned} \tag{2}$$

where ε_0 is the on-site energy, $C^{+}_{i\alpha}$ and $C_{i\alpha}$ are the creation and annihilation operators for an electron with spin α at site i, t is the nearest-neighbor hopping parameter, λ denotes the strength of intrinsic SOC, $\boldsymbol{S}$ represents the spin Pauli matrices, $\boldsymbol{d}_{ki}$ denotes the vector from site i to site k, and M corresponds to the exchange field. As shown in Figs. 2(a) and 2(e), the material remains unpolarized in the absence of SOC, with the system residing in a non-valley-polarized state. However, because Pt is a heavy transition metal, its crystal field generates strong SOC, which significantly modifies the band structure, as illustrated in Figs. 2(b) and 2(f).

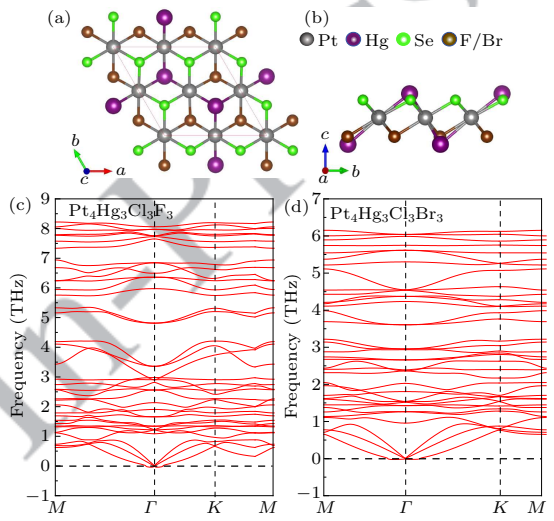


Fig. 1. (a)–(b) Side and top views of the unit cell structure of monolayer $\mathrm{Pt_4Hg_2Cl_3Br_3}$. (c)–(d) Phonon dispersion of the 2D lattice.

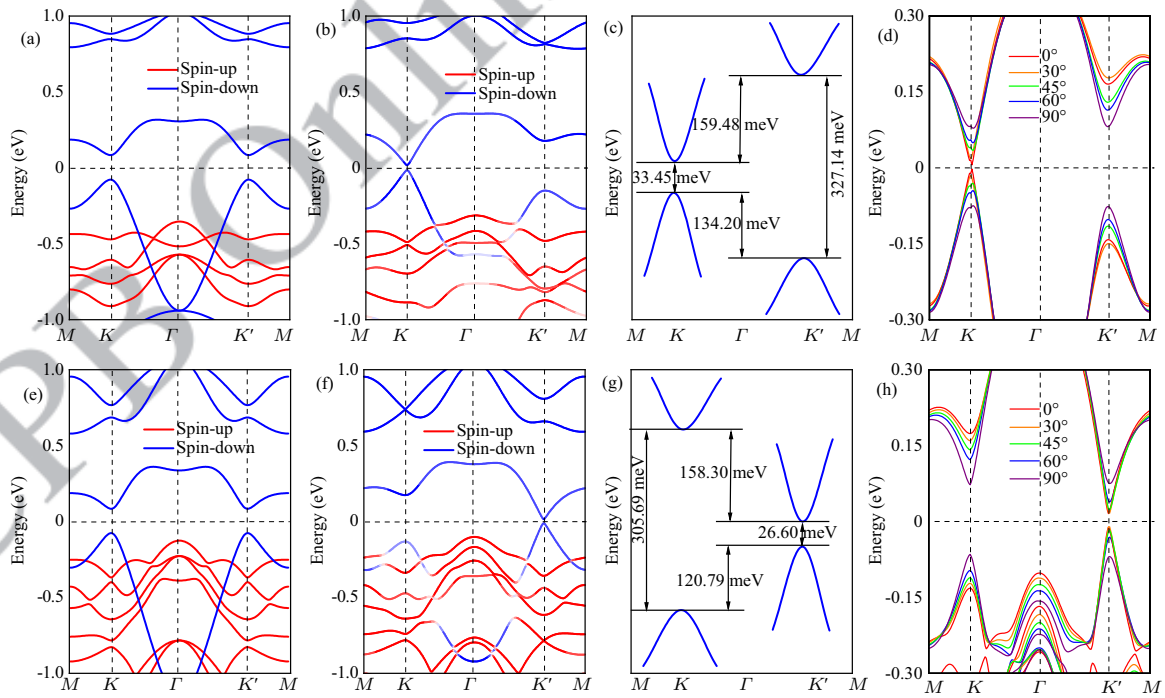


Fig. 2. Band structures of $\mathrm{Pt_4Hg_2Cl_3F_3}$ [(a)–(d)] and $\mathrm{Pt_4Hg_2Cl_3Br_3}$ [(e)–(h)]. (a) and (e) PBE band structures without SOC. (b) and (f) PBE band structures with SOC. (c) and (g) Band gap schematics. (d) and (h) Band structures with the magnetic axis rotated from the z-axis to the x-axis, where θ is the angle between the two axes.

The degeneracy between the K and K' valleys is lifted, leading to energy splitting and the emergence of valley polarization. More interestingly, the exchange field breaks time-reversal symmetry and induces a nonzero Chern number, thereby realizing the QAVHE. Strain engineering provides an additional degree of control, enabling band inversion and topological phase transitions, thus further tuning valley-polarized transport. Fundamentally, this TB model suggests that incor-

CPB Online First

porating heavier elements as functional groups can enhance the SOC-induced bandgap, offering a practical strategy for designing large-gap QAH states in future materials. Such multifreedom tunability endows $Pt_4Hg_2Cl_3X_3$ with potential applications in low-power electronic devices. Moreover, the chiral propagation of edge states supports dissipationless current transport, providing a promising route toward constructing highly efficient quantum transport channels.

We further investigated the magnetic properties of $Pt_4Hg_2Cl_3X_3$ (X = F, Br). To determine the magnetic ground state, four possible spin configurations were considered: Néel antiferromagnetic (NAFM), stripe antiferromagnetic (SAFM), zigzag antiferromagnetic (ZAFM), and ferromagnetic (FM). Quantitative calculations were performed using a supercell, and the total energy analysis reveals that the FM configuration is energetically more favorable than the NAFM, SAFM, and ZAFM states. The energy difference between the FM and AFM states is defined as ($\Delta E = E_{\mathrm{FM}} - E_{\mathrm{AFM}}$). For $Pt_4Hg_2Cl_3F_3$ and $Pt_4Hg_2Cl_3Br_3$, the ΔE values are 51.64 meV and 113.65 meV, respectively, confirming that the FM state is the magnetic ground state. The corresponding magnetic moment is 6 μ_{B} per unit cell. According to the nearest-neighbor Heisenberg model, the Curie temperature T_{c} can be estimated by the relation $3k_{\mathrm{B}}T_{\mathrm{c}}/2 = (E_{\mathrm{FM}} - E_{\mathrm{AFM}})/N$, where k_{B} is the Boltzmann constant and N is the number of magnetic atoms in the supercell. Using this approach, the Curie temperatures of $Pt_4Hg_2Cl_3F_3$ and $Pt_4Hg_2Cl_3Br_3$ are obtained as 99.9 K and 219.7 K, respectively. These results demonstrate that $Pt_4Hg_2Cl_3X_3$ is intrinsically ferromagnetic and indicate that its magnetic ordering is expected to persist up to room temperature.

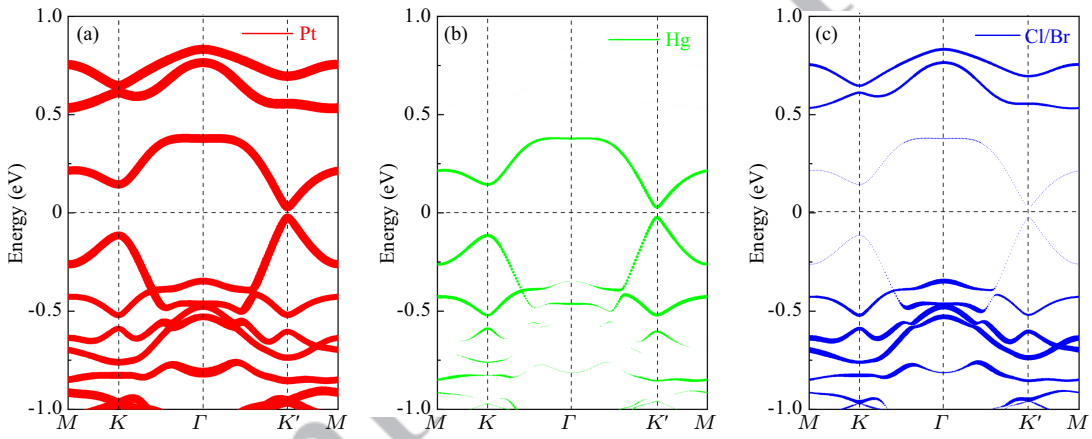


Fig. 3. Atomic-projected component analysis of 2D $Pt_4Hg_2Cl_3Br_3$.

Based on the similarity of the ferromagnetic (FM) ground-state structures of $Pt_4Hg_2Cl_3F_3$ and $Pt_4Hg_2Cl_3Br_3$, $Pt_4Hg_2Cl_3F_3$ is described in detail in the ESI, and $Pt_4Hg_2Cl_3Br_3$ is taken as a representative example for further discussion. First, we computed the PBE band structure of 2D $Pt_4Hg_2Cl_3Br_3$ without spin–orbit coupling (SOC). As shown in Fig. 2(e), the calculation yields a band gap of 160.12 meV. We also recalculated the band structure using the HSE06 hybrid functional (Fig. S2(b)), which gives a band gap of 1.23 eV. The similar band-structure profiles obtained from these two methods confirm the reliability of the PBE description of the electronic states when appropriate correlation corrections (U) are included. $Pt_4Hg_2Cl_3Br_3$ is identified as a direct-gap semiconductor, with the valence-band maximum located at the degenerate K and K' points. This indicates that, in the absence of SOC, the system remains valley-degenerate. However, owing to the large atomic mass of Pt and the crystal-field environment, SOC is strong in this system. Upon inclusion of SOC, the band structure undergoes significant modification: the degeneracy between the K and K' valleys is lifted, producing an energy splitting between the two valleys (*i.e.*, valley polarization), as shown in Fig. 2(f). A schematic diagram of the valley-split gaps is presented in Fig. 2(g). After the degeneracy is lifted, the optical band gaps at K and K' are 305.69 meV and 26.60 meV, respectively, while the valley polarization values in the conduction and valence bands are 158.30 meV and 120.79 meV, respectively. An important feature of this 2D ferrovalley system is that the valley polarization reverses when the magnetization axis is switched. For 2D $Pt_4Hg_2Cl_3Br_3$, reversing the magnetization from $+z$ to $-z$ interchanges the optical gaps at K and K', as confirmed in Fig. 5(h). Figure 2(h) shows the evolution of the electronic band structure as the magnetic axis is rotated from the out-of-plane (z) direction to the in-plane (x) direction. During this rotation, the optical gaps at K and K' converge and eventually become degenerate when the magnetization lies in-plane, resulting in the disappearance of valley polarization. This behavior indicates that, with SOC and an out-of-plane magnetization axis, the system enters a ferrovalley state; conversely, rotating the magnetization into the plane suppresses the valley polarization and restores the valley-degenerate (nonpolarized) state. To further elucidate the electronic states of the 2D $Pt_4Hg_2Cl_3Br_3$

CPB Online Press

lattice, we performed atomic-projected component analyses, as shown in Fig. 3. The results clearly indicate that the states contributing to the valleys near the Fermi level arise primarily from Pt atoms, with Hg atoms making a secondary contribution; the contributions from Cl and Br atoms are comparatively minor.

Having confirmed that the valence and conduction-band contributions originate mainly from Pt and Hg, we further plotted orbital-projected component analyses for Pt and Hg (Fig. 4). The orbital projections show that states near the Fermi level are principally derived from Pt d orbitals and the s orbital of Hg. Specifically, among the Pt d orbitals, the d_{xz} and d_{yz} components dominate, followed by d_{xy} and $d_{x^2-y^2}$,; the contribution of the Pt d_{z^2} orbital near the Fermi level is negligible.

We calculated the magnetic anisotropy energy (MAE) of the unit cell along different crystallographic axes. The energy difference between the in-plane and out-of-plane orientations $(\mathrm{MAE} = E_{\mathrm{IP}} - E_{\mathrm{OP}})$ is −6.18 meV. This indicates that the in-plane configuration has a slightly lower anisotropy energy surface, suggesting that the easy magnetization axis preferentially lies within the plane. However, when the magnetic axis is in-plane, the material remains in a non-valley-polarized state since the K and K' valleys are degenerate and no valley polarization occurs. To explore external modulation, we employed strain engineering, which is regarded as one of the most effective experimental methods for tuning the electronic properties of 2D materials. In this work, biaxial strain (both tensile and compressive) was applied to the $Pt_4Hg_2Cl_3Br_3$ lattice. The strain is defined as $\varepsilon = (a - a_0)/a_0$, where a and a_0 represent the strained and unstrained lattice constants, respectively.[58–63] As shown in Fig. 5(a), the total energy of the $Pt_4Hg_2Cl_3Br_3$ lattice reaches a minimum without applied strain. Figures 5(b) and 5(c) illustrate the evolution of the magnetic ground state and MAE under biaxial strain. The results show that the FM ground state is robust against both tensile and compressive strains, indicating strong stability of the ferromagnetic order. Regarding the MAE, the in-plane anisotropy gradually decreases as the strain changes from compressive to tensile. When the tensile strain reaches 8%, the magnetic easy axis switches from in-plane to out-of-plane, demonstrating a strain-induced magnetic anisotropy phase transition. This confirms that strain engineering can effectively tune the easy axis of $Pt_4Hg_2Cl3Br_3$ from in-plane to out-of-plane. The electronic band structure under 8% tensile strain is shown in Fig. 5(d). As shown in Fig. 5(e), the valley characteristics remain unchanged, but the degeneracy at the K and K' valleys is lifted, resulting in valley splitting. The optical bandgaps at the K and K' valleys are 259.5 meV and 51.97 meV, respectively, with valley polarization values of 115.9 meV and 91.6 meV for the conduction and valence bands. Compared with the unstrained case in Fig. 2(e), the global bandgap increases while the valley polarization is only slightly affected by tensile strain, which is advantageous for device applications. Moreover, as illustrated in Fig. 5(f), reversal of the magnetic axis and the corresponding reversal of valley polarization can also be achieved by applying an external magnetic field.

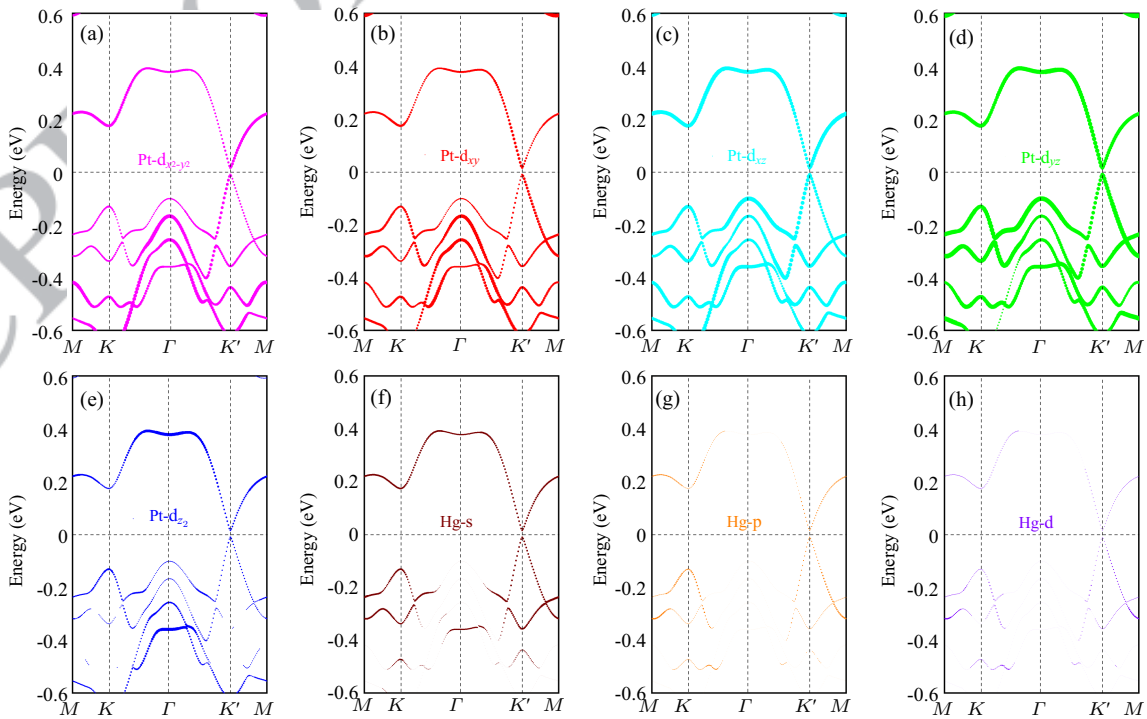


Fig. 4. Orbital-projected band-component analysis of 2D $Pt_4Hg_2Cl_3Br_3$.

CPL Online in Press

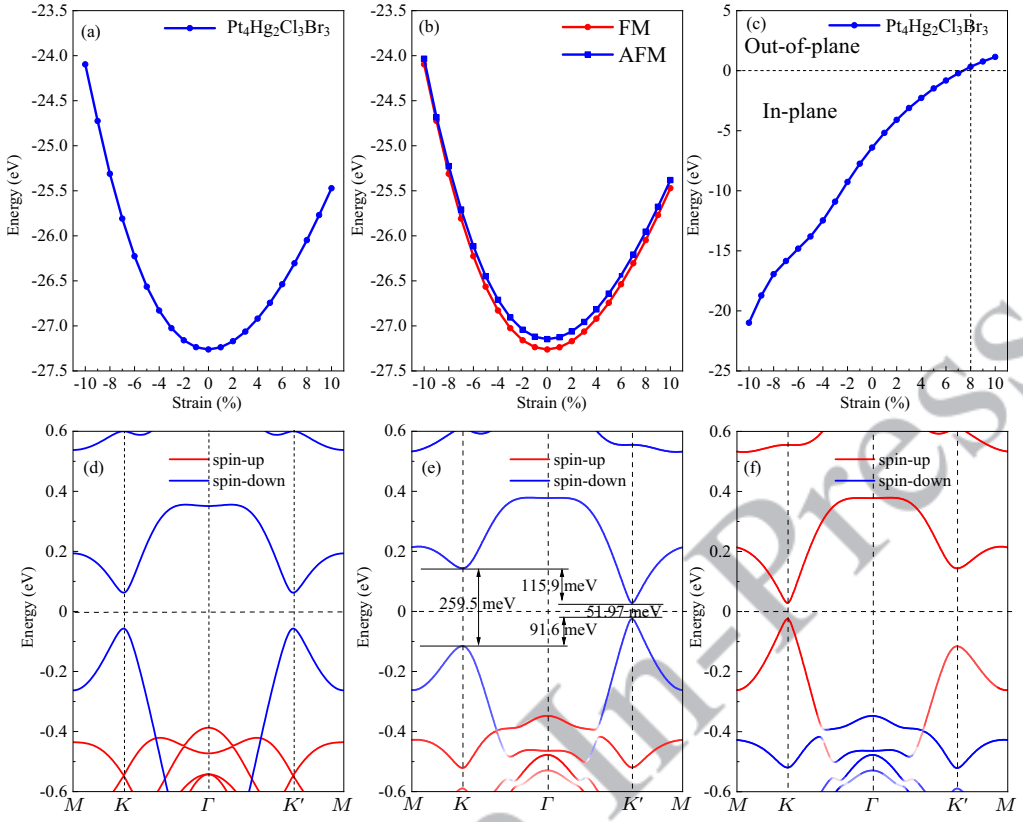


Fig. 5. (a)–(c) Electronic properties of monolayer $Pt_4Hg_2Cl_3Br_3$ under biaxial strain. (a)–(c) Strain-dependent evolution of the total energy, the energy difference between ferromagnetic and antiferromagnetic states, and the magnetic anisotropy energy. (d)–(f) PBE electronic band structures under 8% tensile strain: (d) without SOC, (e) with SOC, and (f) with SOC when the magnetic axis is along the $-z$ direction.

To further verify the existence of the quantum anomalous valley Hall effect (QAVHE) in the 2D $Pt_4Hg_2Cl_3Br_3$ lattice, we conducted calculations of the Berry curvature using the following formula:[64]

$$\Omega(k) = \sum_n f_n \Omega_z(k), \tag{3}$$

$$\Omega_z(k) = -2 \sum_{n' \neq n} Im \frac{\langle \psi_{nk} | \upsilon_x | \psi_{n'k} \rangle \langle \psi_{n'k} | \upsilon_y | \psi_{nk} \rangle}{(\varepsilon_{n'k} - \varepsilon_{nk})^2}, \tag{4}$$

where n is the band index, ψ_{nk} is the eigenstate of eigenvalue ε_{nk} of band n, f_n is the Fermi distribution function, and υ is the velocity operator. By integrating $\Omega_z(k)$ over the first Brillouin zone (BZ), the Chern number (C) can be obtained by[65,66]

$$C = \frac{1}{2\pi} \sum_n \int_{BZ} d^2k \Omega_z(k). \tag{5}$$

The calculated Berry curvature of 2D $Pt_4Hg_2Cl_3Br_3$ is presented in Figs. 6(a) and 6(b). The system exhibits intrinsic ferromagnetism, and the Berry curvature $\Omega_z(k)$ has the same sign at both the K and K' valleys, although their absolute values differ. From the band structure in Fig. 2(f) and the Berry curvature distribution in Figs. 6(a) and 6(b), it can be seen that the optical bandgap (ΔK) at the K valley is larger than that at the K' valley. Nevertheless, the Berry curvature $\Omega_z(k)$ at the K valley is smaller than $\Omega_z(k)$ at the K' valley. This inverse relationship is explained by the Kubo formula, which states that the Berry curvature is inversely proportional to the square of the valley bandgap. Hence, the main numerical contributions to the Berry curvature arise from the band edges at the K and K' valleys. Interestingly, the Berry curvature distribution of $Pt_4Hg_2Cl_3Br_3$ differs significantly from that of conventional ferrovalley materials, in which the Berry curvatures at K and K' have opposite signs. In contrast, for 2D $Pt_4Hg_2Cl_3Br_3$ the Berry curvatures at both valleys share the same sign. To further clarify this unusual feature, we calculated the edge-state spectrum and anomalous Hall conductivity, as presented in Figs. 6(c) and 6(d).

The formula for the anomalous Hall conductivity is given by[24,67]

$$\sigma_{xy}^i = -\frac{e^2}{h} \frac{1}{2\pi} \int_{BZ} d^2k \Omega_z(k). \tag{6}$$

By integrating the Berry curvature over the first Brillouin zone, we calculated the Chern number and obtained Chern number $C = 1$. The quantum anomalous Hall conductivity calculated within the spin-down band gap between the valence-band edge and the conduction band exhibits a quantized plateau with a value of $\sigma_{xy} = Ce^2/h$. Furthermore, the local density of states (LDOS) at the boundary was evaluated by solving the imaginary part of the Green's function, as illustrated in Fig. 6(c). The results reveal the presence of a chiral edge state bridging the conduction-band minimum and the valence-band max-

CPB Online-In-Press

imum in the bulk gap, consistent with the topological property of $C = 1$. These findings confirm that the 2D ferrovalley material $Pt_4Hg_2Cl_3Br_3$ is not only intrinsically ferromagnetic but also a topological insulator, exhibiting the QAHE. More importantly, the coexistence of valley polarization and the QAHE in the same system demonstrates the realization of the QAVHE. This work therefore enriches the family of 2D ferrovalley materials and broadens the scope of systematic investigations into their quantum properties. The demonstrated QAVHE further highlights the application potential of $Pt_4Hg_2Cl_3Br_3$ in valleytronics, spintronics, and topological nanoelectronics.

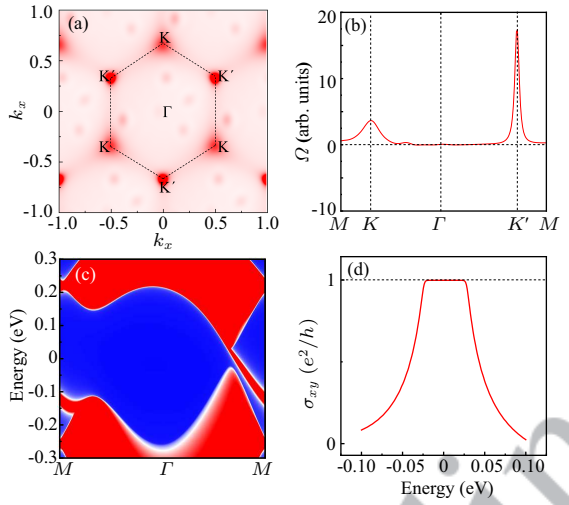


Fig. 6. Berry curvature distribution of $Pt_4Hg_2Cl_3Br_3$ in the 2D Brillouin zone under 8% biaxial strain. (b) Berry curvature along high-symmetry lines. (c) Edge-state density of $Pt_4Hg_2Cl_3Br_3$ under 8% strain. (d) Anomalous Hall conductivity under 8% strain.

4. Conclusion

In summary, based on first-principles calculations within density functional theory, we have proposed a novel 2D ferrovalley material, $Pt_4Hg_2Cl_3X_3$ (X = F, Br). A comprehensive investigation of its electronic structure, stability, magnetism, band structure, and topological properties has been carried out. Our results demonstrate that the intrinsic ferromagnetism of $Pt_4Hg_2Cl_3X_3$ breaks both spatial mirror symmetry and time-reversal symmetry, thereby providing the fundamental condition for spontaneous valley polarization. When spin–orbit coupling (SOC) is included and the magnetic easy axis is oriented out-of-plane, the valley degeneracy is lifted, leading to the emergence of spontaneous valley polarization. Further analyses of the Berry curvature, anomalous Hall conductivity, and edge-state spectrum confirm that the system hosts a nontrivial topological phase, realizing the QAVHE. Moreover, under biaxial tensile strain, the magnetic easy axis undergoes a transition from in-plane to out-of-plane. These findings not only enrich the family of ferrovalley materials but also establish a promising material platform for achieving the QAVHE. The rich coupling among valley, spin, and electronic degrees of freedom, together with multiple Hall effects, highlights the potential of $Pt_4Hg_2Cl_3X_3$ in valleytronics, spintronics, and topological nanoelectronics.

Acknowledgements

Project supported by Independent Cultivation Program of Innovation Team of Jinan City (Grant No. 2021GXRC043), the National Natural Science Foundation of China (Grant No. 52173283), and the Natural Science Foundation of Shandong Province, China (Grant No. ZR2025MS4).

References

[1] Schaibley J R, Yu H Y, Clark G, Rivera P, Ross J S, Seyler K L, Yao W and Xu X D 2016 *Nat. Rev. Mater.* 16055
[2] Wolf S A, Awschalom D D, Buhrman R A, Daughton J M, Molnar S von, Roukes M L, Chtchelkanova A Y and Treger D M 2001 *Science* **294** 1488
[3] Xiao D, Yao W and Niu Q 2007 *Phys. Rev. Lett.* **99** 236809
[4] Zhang S J, Zhang C W, Zhang S F, *et al.* 2017 *Phys. Rev. B* **96** 205433
[5] Xiao D, Liu G B, Feng W, Xu X and Yao W 2012 *Phys. Rev. Lett.* **108** 196802
[6] Liu Y, Gao Y, Zhang S, He J, Yu J and Liu Z 2019 *Nano Res.* **12** 2695
[7] Splendiani A, Sun L, Zhang Y, Li T, Kim J, Chim C Y, Galli G and Wang F 2010 *Nano Lett.* **10** 1271
[8] Eftekhari A 2017 *J. Mater. Chem. A* **5** 18299
[9] Radisavljevic B, Radenovic A, Brivio J, Giacometti V and Kis A 2011 *Nat. Nanotechnol.* **6** 147
[10] Li S S, Ji W X, Hu S J, Zhang C W and Yan S S 2017 *ACS Appl. Mater. Inter.* **9** 41443
[11] Wang Y P, Ji W X, Zhang C W, *et al.* 2017 *Appl. Phys. Lett.* **110** 213101
[12] Pan H, Li Z, Liu C C, Zhu G, Qiao Z and Yao Y 2014 *Phys. Rev. Lett.* **112** 106802
[13] Ding J, Qiao Z, Feng W, Yao Y and Niu Q 2011 *Phys. Rev. B* **84** 195444
[14] Wu S, Ross J S, Liu G B, Aivazian G, Jones A, Fei Z, Zhu W, Xiao D, Yao W, Cobden D and Xu X D 2013 *Nat. Phys.* **9** 149
[15] Zeng H, Dai J, Yao W, Xiao D and Cui X 2012 *Nat. Nanotechnol.* **7** 490
[16] Ye Z L, Sun D Z and Heinz T F 2017 *Nat. Phys.* **13** 26
[17] Mak K F, He K, Shan J and Heinz T F 2012 *Nat. Nanotechnol.* **7** 494
[18] Cheng Y C, Zhang Q Y and Schwingenschlögl U 2014 *Phys. Rev. B* **89** 155429
[19] Peng R, Ma Y, Zhang S, Huang B and Dai Y 2018 *J. Phys. Chem. Lett.* **9** 3612
[20] Singh N and Schwingenschlogl U 2017 *Adv. Mater.* **29** 1600970
[21] Xu L, Yang M, Shen L, Zhou J, Zhu T and Feng Y P 2018 *Phys. Rev. B* **97** 041405
[22] Wang B J, Sun Y Y, Chen J, Ju W W, An Y P and Gong S J 2021 *J. Mater. Chem. C* **9** 3562
[23] Seyler K L, Zhong D, Huang D, Linpeng X, Wilson N P, Taniguchi T, Watanabe K, Yao W, Xiao D, McGuire M A, Fu K C and Xu X 2018 *Nano Lett.* **18** 3823
[24] Cai T, Yang S A, Li X, Zhang F, Shi J, Yao W and Niu Q 2013 *Phys. Rev. B* **88** 115140
[25] MacNeill D, Heikes C, Mak K F, Anderson Z, Kormanyos A, Zolyomi V, Park J and Ralph D C 2015 *Phys. Rev. Lett.* **114** 037401
[26] Zhang X X, Cao T, Lu Z, Lin Y C, Wang Y, Li Z, Hone J C, Robinson J A, Smirnov D, Louie S G and Heinz T F 2017 *Nat. Nanotechnol.* **12** 883
[27] Srivastava A, Sidler M, Allain A V, Lembke D S, Kis S and Imamoğlu A 2015 *Nat. Phys.* **11** 141
[28] Rycerz A, Tworzydło J and Beenakker C W J 2007 *Nat. Phys.* **3** 172
[29] Gunlycke D and White C T 2011 *Phys. Rev. Lett.* **106** 136806
[30] An X T, Xiao J, Tu M W Y, *et al.* 2017 *Phys. Rev. Lett.* **118** 096602
[31] An X T and Yao W 2020 *Phys. Rev. Appl.* **14** 014039
[32] Wu B, Song Y, Ji W, *et al.* 2023 *Phys. Rev. B* **107** 214419
[33] Sun H, Li S S, Ji W, *et al.* 2022 *Phys. Rev. B* **105** 195112
[34] Hu H, Tong W Y, Shen Y H, *et al.* 2020 *npj Comput. Mater.* **6** 129
[35] Zhou X, Zhang R W, Zhang Z, *et al.* 2021 *npj Comput. Mater.* **7** 160

CPB Online First Press

[36] Li S, Wang Q, Zhang C, *et al.* 2021 *Phys. Rev. B* **104** 085149
[37] Feng X, Xu X, He Z, *et al.* 2021 *Phys. Rev. B* **104** 075421
[38] Guo S D, Zhu J X, Yin M Y, *et al.* 2022 *Phys. Rev. B* **105** 104416
[39] Huan H, Xue Y, Zhao B, *et al.* 2021 *Phys. Rev. B* **104** 165427
[40] Longuinhos R, Vymazalová A, Cabral A R, *et al.* 2020 *Journal of Raman Spectroscopy* **51** 357
[41] Facio J I, Das S K, Zhang Y, *et al.* 2019 *Phys. Rev. Mater.* **3** 074202
[42] Bafekry A, Stampfl C, Nguyen C, *et al.* 2020 *Phys. Chem. Chem. Phys.* **22** 24471
[43] Liu Z, Han Y, Ren Y, *et al.* 2021 *Phys. Rev. B* **104** L121403
[44] Rehman M U, Kiani M and Wang J 2022 *Phys. Rev. B* **105** 195439
[45] Kresse G and Hafner J 1993 *Phys. Rev. B* **47** 558
[46] Kresse G and Furthmüller J 1996 *Phys. Rev. B* **54** 11169
[47] Kresse G and Furthmüller J 1996 *Comput. Mater. Sci.* **6** 15
[48] Parr R G and Yang W 1989 *Density-Functional Theory of Atoms and Molecules* (New York: Oxford University Press) pp. 5–15
[49] Fischetti M V and Vandenberghe W G 2016 *Phys. Rev. B* **93** 155413
[50] Calderon C E, Plata J J, Toher C, *et al.* 2015 *Comput. Mater. Sci.* **108** 233
[51] Brouder C, Panati G, Calandra M, *et al.* 2007 *Phys. Rev. Lett.* **98** 046402
[52] Sancho M P L, Sancho J M L, Sancho J M L, *et al.* 1985 *J. Phys. F: Metal Phys.* **15** 851
[53] Bafekry A, Obeid M M, Nguyen C V, *et al.* 2020 *J. Mater. Chem. A* **8** 13248
[54] Zhou M, Ming W, Liu Z, *et al.* 2014 *Proc. Natl. Acad. Sci. USA* **111** 14378
[55] Zhou M, Ming W, Liu Z, Wang Z, Yao Y and Liu F 2014 *Sci. Rep.* **4** 7102
[56] Wu C, Bergman D, Balents L and Das Sarma S 2007 *Phys. Rev. Lett.* **99** 070401
[57] Jungwirth T, Niu Q and MacDonald A H 2002 *Phys. Rev. Lett.* **88** 207208
[58] You B, Tang M T, Tsai C, *et al.* 2019 *Adv. Mater.* **31** 1807001
[59] Dai Z, Liu L and Zhang Z 2019 *Adv. Mater.* **31** 1805417
[60] Desai S B, Seol G, Kang J S, *et al.* 2014 *Nano Lett.* **14** 4592
[61] He K, Poole C, Mak K F, *et al.* 2013 *Nano Lett.* **13** 2931
[62] Wang J, He L, Zhang Y, *et al.* 2024 *Adv. Mater.* **36** 2314145
[63] Nie Y, Rahman M, Wang D, *et al.* 2015 *Sci. Rep.* **5** 17980
[64] Thouless D J, Kohmoto M, Nightingale M P and den Nijs M 1982 *Phys. Rev. Lett.* **49** 405
[65] Yao Y, Kleinman L, MacDonald A H, *et al.* 2004 *Phys. Rev. Lett.* **92** 037204
[66] Wang M L, Li S S, Wang Y P, *et al.* 2025 *Phys. Rev. B* **112** 174414
[67] Li R, Jiang J, Mi W and Bai H 2021 *Nanoscale* **13** 14807

CPB Online In-Press